Nested Closed-loop Control of Quasi-Static MEMS Scanners with Large Dynamic Range

Paolo Frigerio, Luca Molinari, Andrea Barbieri, Marco Zamprogno, Gianluca Mendicino, Nicolò Boni, and Giacomo Langfelder, *IEEE Member*

***Abstract*—This research discusses the challenges in implementing a fully electrical closed-loop control system for high-end applications of quasi-static microscanners, accounting at the same time for wide aperture, high-accuracy and wide-bandwidth. The discussion highlights how not only the ringing of the main mode, but also the presence of spurious modes and nonlinearity, impact the closed loop stability and accuracy. A novel control approach based on nested loops is conceived and implemented in the digital domain in a mixed-signal application-specific integrated circuit (ASIC). The developed versatile ASIC is designed to be coupled to different types of micromirrors, with fundamental frequency ranging from few hundred Hz to few kHz, by simply adjusting coefficients in the digital domain. The ASIC is here successfully operated with two micromirrors and results demonstrate saw-tooth position control at 28-32 deg field of view and up to 120 Hz refresh rate, while holding at the same time a tilt angle resolution of 25 mdeg r.m.s. (dynamic range of 60 dB) and a linearity error below ±1%.**

***Index Terms*—MEMS, micromirrors, pico-projectors, AR, VR, closed-loop, control systems.**

I. Introduction

MEMS (Micro Electro Mechanical System) micromirrors are becoming a fundamental component in LiDAR applications [1] and raster-scanning systems for Augmented Reality (AR) and Virtual Reality (VR) applications, ranging from pico-projectors, to smart glasses and Head-Up Displays (HUD) [2], [3]. In such systems, the projected image is constructed by a triplet of modulated laser beams steered either by a biaxial mirror [4]–[6] or by two monoaxial mirrors [7], [8] that perform a scan along both image dimensions.

In a dual-mirror system, the horizontal scan is performed by a so-called "resonant" scanner [9]. As the name implies, the device is actuated at its resonance frequency, typically in the order of tens of kHz to satisfy the horizontal resolution requirements [10]. The dimensions of such devices are typically limited to a diameter in the order of $1\,\mathrm{mm}$ to minimize diffraction effects [11].

Manuscript received Month xx, 2xxx; revised Month xx, xxxx; accepted Month x, xxxx.

Paolo Frigerio and Giacomo Langfelder are with the Department of Electronics, Information and Bioengineering, Politecnico di Milano, Milan, 20133, Italy (phone: 02-2399-3744; e-mail: paolo.frigerio@polimi.it).

Luca Molinari, Andrea Barbieri, Marco Zamprogno, Gianluca Mendicino and Nicolò Boni are with STMicroelectronics, Cornaredo (MI), 20010, Italy.

The vertical scan, on the contrary, is performed by a much larger mirror (diameters in the order of few mm), which has to accommodate the entire horizontal scan line reflected by the master resonant mirror. Such device, referred to as "quasi-static" or "linear" scanner in the following, is actuated with sawtooth or triangular signals [12] having a frequency matched to the desired refresh rate, e.g. $60\,\mathrm{Hz}$ for a typical display.

As a consequence of their large size, and the required large rotational compliance, the resonance frequency of these devices is typically small, i.e. in the order of hundreds of Hz up to few kHz [11], with air drag damping [13] yielding a quality factor in the order of 100. These two parameters produce band-like distortions of the image due to ringing of the mirror tilt angle, caused by excitation of the mechanical resonance by the high-order harmonics of the driving signal [12]. Providing an accurate and versatile solution to this issue is the subject of this research, with a focus on scanners equipped with piezoelectric actuators and an embedded piezoresistive position sensor.

The performance of the control system is gauged mainly by: the maximum field-of-view (FOV), i.e. the maximum tilt angle achieved by the mirror, which is strictly related to the vertical resolution; the linearity of the trace, i.e. any distortion with respect to a straight line; the r.m.s. noise, affecting the positioning of each pixel [11], [14], [15]. The target system specifications for this work are those of next generation displays: a FOV larger than $28°$, a linearity error within $1\,\%$, noise within $10\,\mathrm{m}°$, and a minimum $60\,\mathrm{Hz}$ refresh rate [10]–[12].

In the past years, different open-loop driving techniques for linear scanners have been proposed, their main advantage being the reduced area occupation due to the absence of an embedded position sensor. In [16] Schitter proposed a shaping of the driving signal consisting in "flattening" the peaks, in order to suppress the effect of mechanical resonance. In [17] Janschek proposed the design of an adaptive prefilter, coupled to a resistive current-limiting feedback, applied to a comb-driven electrostatic scanner to both suppress resonance and compensate for the intrinsic non-linearity of staggered vertical combs. In [18] Schroedter showed that limitation of jerk (i.e., the third derivative of displacement) can be applied to previous open-loop techniques [19] in order to minimize residual oscillations.

A review of closed-loop control strategies is discussed in [20], all based on optical position sensors. In [21] again Schroedter showed an extension to previous open-loop techniques by using a state observer, enabled by an optical Position

Sensitive Detector, to improve overall system robustness and further reduce positioning errors. In [22] he also showed that the same concept can be implemented using an embedded piezoresistive sensor, thus avoiding the area occupation required by the optical sensor. In [6] Tsai showed the effectiveness of a simple feedback technique for the slow axis of a 2D microscanner, again exploiting piezoresistive elements in the mirror design. However interesting, all these works focus on electrostatic or electromagnetic scanners, limited by either large voltages [23] or a bulky package. A recent alternative to these technologies is offered by piezoelectric micromirrors, such as [5], but these show a significant coupling of spurious modes to the embedded position sensor, which complicate the closed-loop design. Indeed, as discussed in the following, while piezoelectric actuation offers significant advantages in terms of area and power consumption, it also introduces hysteresis [24], and the actuators typically introduce spurious resonances that are sensed by PZR elements and mistaken for information on the mirror position. Nevertheless, such technology is becoming more and more attractive thanks to its advantages, as shown by recent studies in the field [25]–[28].

This work discusses a novel implementation of a closed-loop system for piezoelectric micromirrors, able to reject the effect of spurious resonances and to control the position of the mirrors up to 32° field-of-view, with a residual linearity error within $\pm 1\,\%$ and noise, referred to the mechanical angle, in the order of $25\,\mathrm{m}^\circ$ rms. Such parameter values are dictated by the evolving need of high-resolution miniaturized scanning systems coping with e.g. HD720 or HD1080 resolution standards [11].

The remainder of the paper is organized as follows: Section II highlights the relevant non-idealities of the MEMS devices that pose a challenge to the closed-loop control design; Section III describes the implementation of the ASIC embedding the mirror control law; Section IV details the conceived control strategies; finally, Section V discusses the experimental results obtained testing two different mirror families.

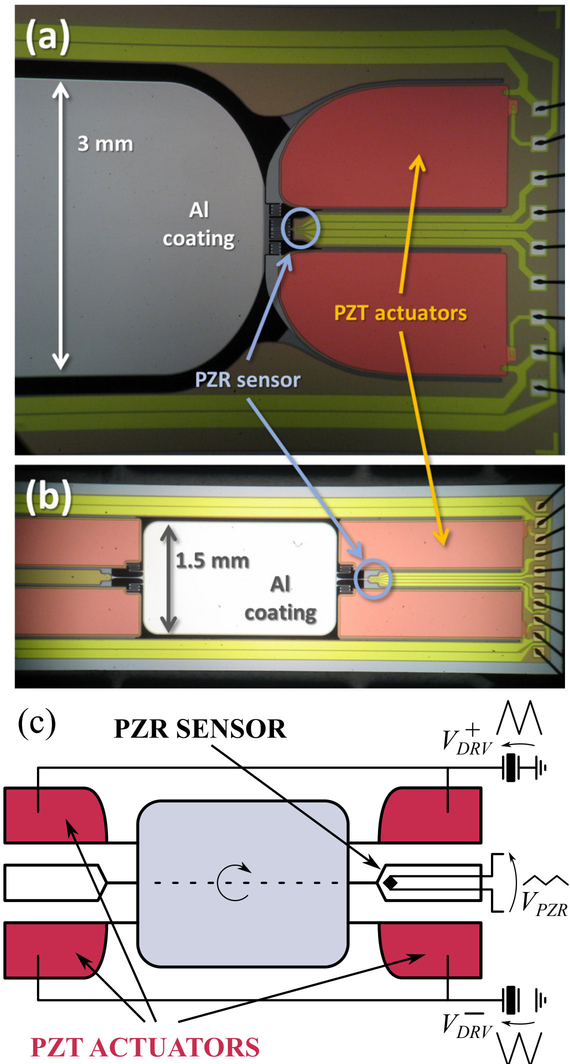

Fig. 1. Picture of two different quasi-static micromirrors, mirror 1 (a) and mirror 2 (b), inspected via optical microscope, along with a schematic view of a micromirror with its actuation and sensing signals (c). The PZT actuators are driven by anti-phase strictly-positive triangular waveforms. The mirror position is readout via an embedded PZR sensor, located close to the anchor point of one of the torsional springs.

II. Non-idealities of the MEMS scanners

This section describes the non-ideal characteristics of the piezoelectric scanners considered in this work, following a brief description of the devices. Such non-idealities are often neglected in the electronics design, such as in [6], but they become relevant for accuracy and stability of a closed-loop control system.

Fig. 1(a)-(b) show two quasi-static micromirrors that were coupled to the developed system and used for experimental validation. Both devices consist of a suspended silicon plate with an aluminium deposition on top to realize the reflective surface. The mass is attached to the substrate by two sets of torsional springs defining the rotation axis, and to four Silicon cantilevers that operate as actuators. On top of these, a 2-μm-thick film of Lead-Zirconate-Titanate (PZT) is deposited between two metal electrodes. The mirror is thus actuated via the converse piezoelectric effect by applying sawtooth voltages to such capacitors with the phases depicted in Fig. 1(c) in order to generate the required tilt. This is in turn sensed by using a set of four diffused piezoresistors (n-type) that are located at the anchor point of one of the torsional springs. For more details about the process and design optimization of such device the reader can refer to [29].

Piezoelectric actuation coupled to piezoresistive sensing enables many significant advantages: PZT requires smaller driving voltages than electrostatic scanners [11]; it shows less linearity with respect to electromagnetic scanners, due to polarization hysteresis [30], but it avoids installation of large permanent magnets [11]; finally, piezoresistive sensing is far more linear than electrostatic sensing, and its temperature dependence, being linear, is easily compensated by trimming the sensitivity against temperature. The main disadvantage of this choice consists in a prominent coupling of mechanical modes to the position sensor, which becomes a significant issue for the stability of a closed-loop system.

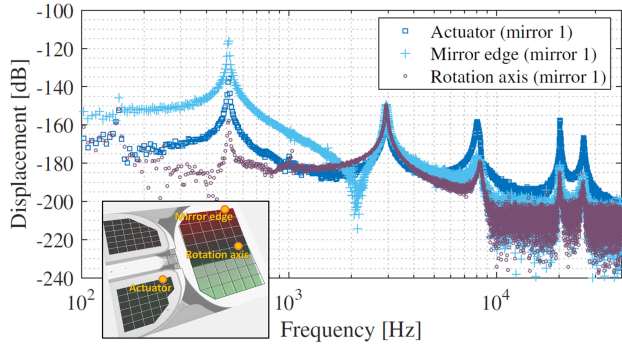

Fig. 2. Open-loop optical characterization of mirror 1. The displacement of the structure is acquired via laser vibrometer for three points on the device, one lying on the rotation axis, one on a PZT actuator and one close to the mirror edge. The bottom-left inset shows the position of these points on the mesh, which is represented for half of the mirror structure.

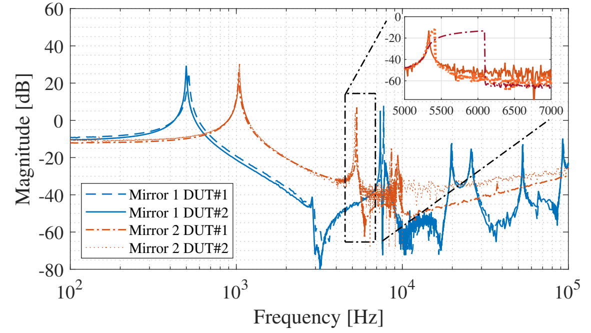

Fig. 3. Transfer functions from PZT to PZR output of four sample devices belonging to two different mirror families. Coupling of spurious modes is clearly visible, with peaks reaching values up to $-20\,\mathrm{dB}$ below the main resonance.

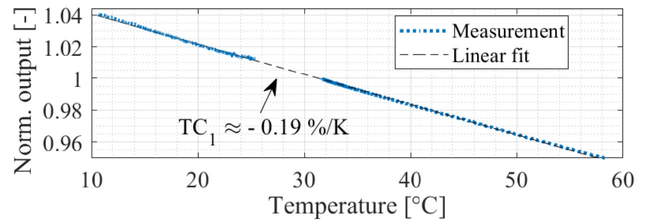

Fig. 4. Temperature dependence of the PZR sensitivity. A linear trend is observed, fitted by a $-0.2\,\%/\mathrm{K}$ coefficient. Missing data around room temperature is due to limitations of the climatic chamber.

Thus, the mirrors are modelled as a multi-resonant system, where only the relevant mechanical modes are considered. Each of the N eigenmodes is represented in the Laplace domain as a second order transfer function as:

$$H_{\vartheta j}(s) = \frac{\vartheta_j(s)}{V_{DRV}(s)} = \frac{\eta_j}{k_{\vartheta j}} \cdot \frac{1}{1 + \frac{s}{\omega_{nj} Q_j} + \frac{s^2}{\omega_{nj}^2}} \tag{1}$$

where η_j is the voltage-to-torque transduction factor, $k_{\vartheta j}$ is the modal stiffness, ω_{nj} and Q_j are the natural frequency and quality factor, respectively, and ϑ_j represents the displacement of the j-th mode (either a translation or a rotation). The mode of interest is the rotational one, corresponding to index j equal to 1 in the following. The output of the piezoresistive sensor is represented as the weighted sum of all the modes:

$$H_{PZR}(s) = \sum_{j=1}^{N} \frac{\eta_j}{k_{\vartheta j}} \cdot \frac{(-1)^{\Gamma_j} \Pi_j}{1 + \frac{s}{\omega_{nj} Q_j} + \frac{s^2}{\omega_{nj}^2}} \tag{2}$$

where the weights Π_j represent the sensitivity of the PZR sensor with respect to each resonant mode, and the exponent Γ_j is determined by the relative phase of the modes.

The reader can imagine that high order eigenmodes do not contribute to a significant rotation of the mirror. Indeed, upon vibrometry inspection, the samples of mirror 1 show the displacement spectrum represented in Fig. 2. The spectrum is shown for three points of the mesh, respectively lying close to the mirror edge, along the axis of rotation and close to the tip of one of the actuators. At low frequencies the rotational mode can be appreciated at about $500\,\mathrm{Hz}$, followed by an out-of-plane translational mode at about $3\,\mathrm{kHz}$. The spectrum of the actuator tip also shows significant peaks at relatively high frequencies, however being absent or much smaller in the spectra of the other two points lying on the mirror surface. Direct comparison with the transfer function measured at the PZR sensor output, reported in Fig. 3 (blue curves), shows that the out-of-plane translation, generating a common-mode signal at the sensor output, is filtered out thanks to the arrangement of the sensor. However, the actuator resonances are also sensed by the piezoresistors as differential modes, resulting in a larger magnitude than that observed at the mirror edge. The figure also shows the transfer function of mirror 2, which is affected by the same issue, although the modes show a different distribution owed to the geometry.

In addition, driving the devices at such large angles (up to 8° of mechanical angle), both the fundamental mode and a few spurious modes show a non-linear behaviour described as a second-order dependence of the modal stiffness on the tilt angle:

$$k_{\vartheta j} = k_{0\vartheta j} + k_{2\vartheta j}\vartheta^2 \tag{3}$$

where $k_{0\vartheta j}$ is the linear contribution and $k_{2\vartheta j}$ is the non-linear one.

Furthermore, the piezoresistive sensor is also affected by a statistical differential offset and by a linear dependence of the sensitivity on temperature. The output differential voltage is thus represented by the equation:

$$V_{out,PZR} = \Pi \cdot (1 + \alpha_\pi \Delta T) + V_{os,PZR} \tag{4}$$

where α_π is the sensitivity temperature coefficient, ΔT is the deviation from calibration temperature, and $V_{os,PZR}$ is the offset voltage. The temperature dependence was acquired by measuring the sensitivity of the device while sweeping the temperature inside a climatic chamber, and it is shown in Fig. 4 on a temperature range spanning $10\,°\mathrm{C}$ to $60\,°\mathrm{C}$. Concerning the offset voltage, as shown in Table I, it is typically larger than the maximum signal, requiring additional care in the electronic front-end design.

The purpose of this work is to design a versatile solution which is able to address all the highlighted issues, while

TABLE I
PARAMETERS OF THE DEVICE FAMILIES UNDER TEST

Symbol	Quantity	Mirror 1	Mirror 2	Units
D	Mirror dimension	3×4	1.44×2.4	mm^2
ω_{n1}	Natural frequency	$2\pi \cdot 500$	$2\pi \cdot 1000$	$\mathrm{rad\,s}^{-1}$
η	PZT efficiency	$2.68 \cdot 10^{-9}$	$5.97 \cdot 10^{-9}$	$\mathrm{N\,m\,V}^{-1}$
Q_1	Quality factor	100	50	–
Π_1	PZR sensitivity	2.7	2.4	$\mathrm{mV/deg}$
ϑ	Target angle	7	8	deg
$V_{PZR,max}$	PZR peak voltage	18.9	21.6	mV
α_π	Temperature coefficient	-0.2	-0.2	$\%\,°\mathrm{C}^{-1}$
$V_{os,PZR}$	PZR offset (1σ)	± 30	± 30	mV
C_{PZT}	PZT capacitance	36	12	nF

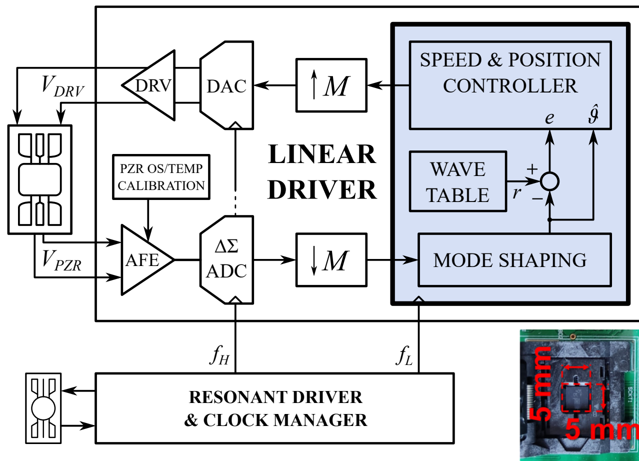

Fig. 5. System-level scheme of the implemented ASIC.

also capable of managing mirrors with different parameters as reported in Table I.

III. ASIC IMPLEMENTATION

The control strategy for the linear mirror is the focus of this work. It is implemented as a custom DSP core within an ASIC that also includes the mirror driver and sensor front-end.

The high-level block scheme of the ASIC is shown in Fig. 5, with the controller core displayed against a light blue background. The triangular position reference, indicating the reference angle to track, is stored in a look-up table, compared to the position signal sensed by the PZR sensor, and processed by the sensing electronics: such signal is amplified by a dedicated analog front-end (AFE), with integrated compensation of both temperature and offset (following an initial calibration); the amplified signal is then converted by a second-order $\Delta\Sigma$ ADC, whose sampling frequency is in the order of a few MHz and whose output is downsampled to the order of hundreds of kHz. The downsampled output is then shaped by a filtering block used to process the high-order spurious resonances. Its output represents a pre-processed angle $\hat{\vartheta}$.

The fully reconfigurable speed and position controller operates on both the pre-processed signal $\hat{\vartheta}$ and the error e calculated with respect to the desired reference r, as described in the next section. The compensated driving signal is then

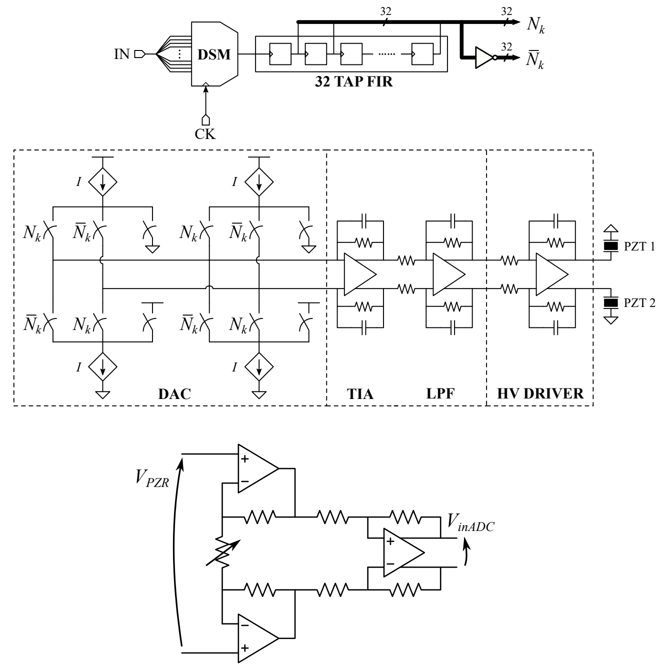

Fig. 6. Schematic of the mirror driver (top) and front-end (bottom).

converted to the analog domain by a current-steering DAC and amplified by a power stage to drive the actuators. The DAC and driver architecture is described in [31], and its schematic is reported in Fig. 6 (top): the driver is a fully-differential amplifier operating at a supply of $40\,\mathrm{V}$. The AFE is also reported in the figure (bottom), and it is implemented as an Instrumentation Amplifier, whose gain resistance is programmable via a set of dedicated registers. The ADC isbased on a II-order mixed-signal sigma-delta topology with a 5 level quantizer, while the downsampling filter is a third-order IIR low-pass filter with programmable bandwidth.

The chip also contains a dedicated driver for the second, resonant, mirror of the raster-scanning system, which also acts as the master clock and generate the two sampling frequencies f_H and f_L used to clock the converters and the digital compensation core. A Phase-Locked Loop (PLL) operates as the clock manager. The dedicated control loop is not discussed in this work, but it is highlighted how the horizontal and vertical axes are synchronized in such a way to avoid de-synchronization due to clock jitter accumulation.

IV. CONTROL STRATEGIES

The controller is implemented by separately facing the issue of stabilizing the tilt angle from the management of spurious resonances, guaranteeing in the end that the combination of the two techniques remains stable.

A. Roll mode control

Considering first the ideal case of a micromirror with no significant mode coupling, the complete control law should be designed in order to accomplish a series of tasks. The primary goal is to create a system close to critical damping (i.e. $Q = 0.5$), in order to eliminate the issue of position

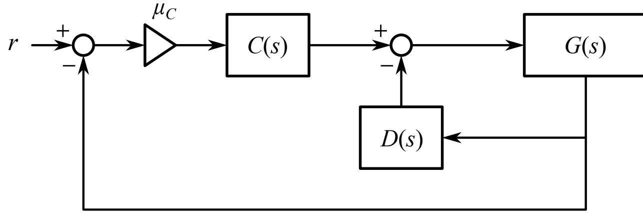

Fig. 7. The adopted control strategy employs two separate controllers, a derivative to control the speed and a position controller operating on the speed-controlled system.

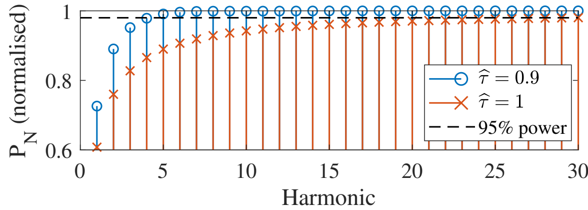

Fig. 8. Sum of the first N harmonics of two sawtooth signals. A shorter retrace time requires a significantly larger bandwidth, thus demanding increased effort to the PZT drivers.

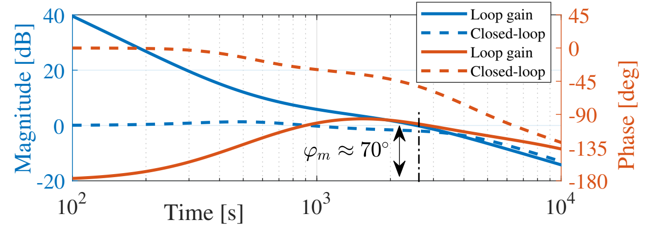

Fig. 9. Ideal sizing of the loop gain for the final solution, with the corresponding closed-loop transfer function. The plots are shown for the system designed on mirror 2, but the same result can be obtained with mirror 1.

ringing and thus its effect in modulating the image brightness. Supporting different applications also demands the capability to set a broad range of bandwidths, with image scanning products requiring actuation signal frequencies ranging from a standard of 60 Hz up to 120 Hz and larger, and a retrace time which should be ideally the shortest possible, such to minimize the loss of overall image brightness. The shorter the retrace, the larger the harmonic content at high frequencies, whose control thus requires an extended bandwidth in order to avoid overshoots at the onset of the trace. It should be noted that, similarly to the effect of ripple, overshoots would result in a brightness modulation along a band of pixels at the top of the image, thus they should be avoided if the goal is to maximize the available scan time. Finally, given the intrinsic non-linear effect of equation (3), an open-loop approach would result in a significant stretch towards the upper and lower portions of the image. Contrarily to the adaptive open-loop approaches discussed in the introduction, this issue is simply solved by the closed-loop system thanks to the linearity of the PZR sensor.

Damping of the roll mode is accomplished by applying a pure derivative controller in the feedback path, as shown in Fig. 7, described by:

$$D(s) = \frac{\mu_D s}{s + \omega_{pD}} \tag{5}$$

where μ_D is the high-frequency gain and ω_{pD} is the pole of the real differentiator stage. The gain is set to achieve a closed loop quality factor of $\sqrt{2}/2$ to maximize the bandwidth:

$$\mu_D = \frac{\sqrt{2}}{\mu_G} \cdot \frac{\omega_{pD}}{\omega_{n1}} \tag{6}$$

where μ_G accounts for the DC gain $H_{PZR}(0)$ and the gain of the PZT driver and PZR front-end.

With such solution, the bandwidth of the resulting closed-loop transfer function is limited by the natural resonance frequency of the device. To quantify this limit, the required bandwidth can be calculated by constructing the reference sawtooth signal via additive synthesis. Given the trace-to-period ratio $\hat{\tau} = T_{rise}/T_{saw}$ for a trace time T_{rise}, the power contained in the first N harmonics is:

$$P_N = \frac{12}{2\pi^4\hat{\tau}^2\left(1-\hat{\tau}\right)^2}\sum_{n=1}^{N}\frac{\sin^2\left(\pi n\hat{\tau}\right)}{n^4}. \tag{7}$$

The plot in Fig. 8 shows the previous equation for two different trace ratios. To maintain 95 % of the total signal power within a frequency range unaffected by a significant phase distortion, an ideal 60 Hz sawtooth signal (orange crosses) would require at least 300 harmonics within a closed-loop bandwidth of 18 kHz, whereas a triangle wave with 90 % trace ratio (blue circles) would require only 50 harmonics within 3 kHz, with an obvious advantage in terms of closed-loop control.

Since a ramp signal is perfectly tracked using a type-II controller, the implementation of the combined speed and position controller of Fig. 5 is the one presented in Fig. 7. The tilt angle controller $C(s)$ is a cascade of two integrators and a phase-lead filter:

$$C(s) = \frac{s + \omega_{zI}}{s} \cdot \frac{s + \omega_{zI}}{s} \cdot \frac{1 + \frac{s}{\omega_{zL}}}{1 + \frac{s}{\omega_{pL}}}. \tag{8}$$

The integrator zeros ω_{zI} and the lead zero ω_{zL} are set at the natural frequency ω_{n1}, and following this choice the bandwidth $\hat{\omega}$ can be arbitrarily set by tuning the gain:

$$\mu_C = \frac{\hat{\omega}}{\omega_{n1}\mu_G}. \tag{9}$$

The pole ω_{pL} is placed at high frequency and is determined by the required phase margin. The loop gain and the closed-loop transfer function are shown in Fig. 9.

The described controllers are implemented as digital filters.

B. Spurious modes control

Considering now the coupling of spurious modes, the issue is tackled by introducing our second order IIR notch filters in the mode shaping block of Fig. 5.

Process spread effects leading to a variation of the resonance frequency in the order of ±10 % is considered for the bandstop design upon preliminary characterization of a few samples.

Furthermore, as shown in the inset of Fig. 3, for a few mechanical structures also the high-order modes may show significant nonlinearity. Thus the resonance frequency of the

j-th nonlinear mode increases with actuation amplitude, according to the following equation:

$$\omega_{nj}(\vartheta) \approx \omega_{nj} \cdot \sqrt{1 + \frac{k_{2\vartheta j}}{k_{0\vartheta j}} \vartheta^2} \tag{10}$$

which determines the centre frequency of the bandstop filters. Thus the effect of spurious resonances is significantly attenuated to preserve the loop stability.

All the modal parameters of the lumped model are derived from FEM analysis of the mechanical structure. The coupling coefficients Π_j, on the other hand, are derived in a one-time family calibration of the devices.

C. Accuracy

High accuracy sets stringent constraints on both the noise and the linearity of the trace. Noise limits the precision in the positioning of all the pixels, whereas linearity, which is defined as the error with respect to a line fit, determines the absolute position of each pixel, and is thus related to distortion effects in the projected image.

The limiting noise sources are the piezoresistors and the AFE noise. The power spectral density of the PZR sensor noise referred to the differential output voltage is:

$$S_{n,PZR}(f) = \frac{K_{fn}}{f} + 4k_B T R_{wb} \approx \frac{K_{fn}}{f} \tag{11}$$

where K_{fn} defines the flicker noise, k_B is the Boltzmann constant, T is temperature and R_{wb} is the nominal value of each resistor. The flicker noise PSD is $(40\mathrm{nV}/\sqrt{\mathrm{Hz}})^2$ at $1\,\mathrm{kHz}$, while the white noise floor is $(7\mathrm{nV}/\sqrt{\mathrm{Hz}})^2$. The AFE input referred noise can be considered white thanks to chopping of the amplifiers, and its density is about $(50\mathrm{nV}/\sqrt{\mathrm{Hz}})^2$. The noise corner is thus about $640\,\mathrm{Hz}$. Flicker noise is the dominant source: indeed considering a target bandwidth of $3\,\mathrm{kHz}$, its contribution on a $10\,\mathrm{s}$ time window is $4\,\mu\mathrm{V}_{\mathrm{rms}}$, larger than the white contribution of $2.4\,\mu\mathrm{V}_{\mathrm{rms}}$. The total integrated noise corresponds to a theoretical error of about $2\,\mathrm{m}^\circ_{\mathrm{rms}}$.

Concerning the loop transfer function, the necessity to introduce notch filters practically reduces the achievable phase margin down to the order of 30°-35°. This leads to an underdamped response that generates a residual overshoot of the step response, which is visible at the end of retrace the more the trace ratio approaches unity. This is especially a problem for mirrors with a low natural frequency. In addition, driving the mirrors at higher frequencies requires increasing the closed-loop bandwidth, although the upper limit set by the mirror zeros can not be exceeded. For such scenarios, a pre-filtering of the driving signal is implemented in order to maximize the usable trace time. This is implemented by calculating the signal table values according to:

$$r[n] = \mathcal{L}^{-1}\left\{ \widetilde{R}(s) \cdot \frac{H_{\vartheta 1,cl}(0)}{H_{\vartheta 1,cl}(s)} \cdot \frac{\widehat{\omega}^2}{(s+\widehat{\omega})^2} \right\} \tag{12}$$

where $H_{\vartheta 1,cl}$ is the real closed-loop transfer function, $\widetilde{R}$ is the Laplace transform of the non-filtered reference sawtooth, and $\widehat{\omega}$ is the target closed-loop bandwidth. As a final remark, this technique could be directly applied to the open-loop response of the mirror, however its effectiveness would be strongly dependent on the matching of both the natural frequency and the native quality factor.

TABLE II
SYSTEM PARAMETERS FOR VARYING RESONANCE FREQUENCIES

f_0 [kHz]	0.4	0.5	1	2	3
ω_{pD} [kHz]	4	5	10	20	30
μ_D	$10\sqrt{2}$	$10\sqrt{2}$	$10\sqrt{2}$	$10\sqrt{2}$	$10\sqrt{2}$
ω_{zL} [kHz]	0.4	0.5	1	2	3
μ_C	7.5	6	3	1.5	1

D. System sizing and limitations

The system is designed to manage multiple mirror families with only one integrated circuit. The sizing of the digital controller is performed accounting for a range of resonance frequencies, from about $400\,\mathrm{Hz}$ up to $3\,\mathrm{kHz}$. The DAC input spans about ± 1, corresponding to an output span of $\pm 2.4\,\mathrm{V}$, and the AFE is designed with a programmable gain to maximize the ADC input dynamics (approximately $\pm 1\,\mathrm{V}$), which leads to digital signals spanning ± 1 after decimation. Thus the controller is always sized considering a unity DC gain, independently of the controlled mirror. Sizing of system parameters depends only on the resonance frequency of the controlled mirror, and is listed in Table II for a target closed loop bandwidth $\widehat{\omega}$ equal to $3\,\mathrm{kHz}$.

The discussed system is, up to our knowledge, the first integrated control system targeted to piezoelectric MEMS mirrors able to both implement the optimal control strategy while also being capable of managing the spurious resonant mode coupling on different mirror families.

The latter consideration also constitutes the main limitation of the proposed solution, which will be addressed in future work. The system effectively relies on an electrical measurement of the mirror position with no optical feedback. Due to the position of the piezoresistive sensor on the device, the angular displacement is corrupted by the actuators displacement. If the notch filters are not properly designed, such spurious information can not be correctly filtered out and may result in spurious high-frequency oscillations appearing superposed to the linear angular displacement and become visible as noise in the projected image. Thus, to compensate for process spread, the proposed system requires at least a family calibration of devices fabricated on the same silicon wafer to identify the frequency of the spurious resonant modes.

V. EXPERIMENTAL RESULTS

As a first step, a validation of the indirect angle estimation obtained from the PZR output is performed through a comparison with a direct measurement of the displacement of the device, obtained using the laser doppler vibrometer (Polytec MSA-500 [32]) shown in Fig. 10(a). The tilt angle is then calculated from the measured displacement x_m as:

$$\vartheta = \tan^{-1}\left(\frac{2x_m}{D}\right) \tag{13}$$

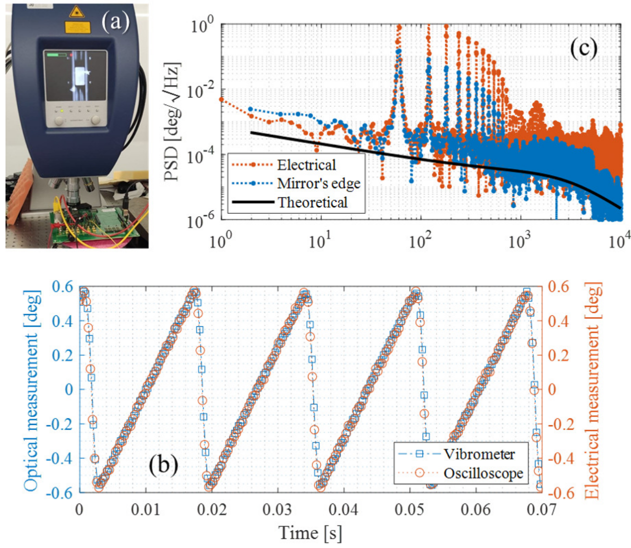

Fig. 10. (a) Photo of the optical setup; (b) comparison between electrical and optical measurement; (c) noise PSD.

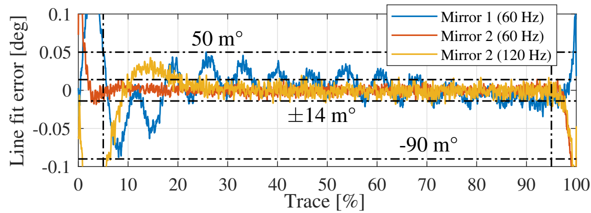

Fig. 11. Comparison between the linearity obtained with both mirrors under test and with different driving frequencies. Stabilization of mirror 1 is much more challenging, given the large number of spurious modes.

where D represents the dimension orthogonal to the rotation axis. Electrical validation, on the other hand, consists in converting the output of the piezoresistive sensor using the corresponding sensitivity Π_1. A direct comparison of the two measurements is then performed, and their good agreement is shown in Fig. 10(b) for mirror 2 actuated with a target angle of only $0.6°$. Such a small value is due to the limited numerical aperture of the vibrometer; however, thanks to such validation, the electrical measurement of the PZR output can be considered reliable for even larger tilt angles.

Fig. 10(c) shows the power spectral density of the optical trace, where it is evident that the flicker noise contribution is dominant within the loop bandwidth. The theoretical power density is also plotted, showing that the measured integrated noise is larger than theoretical predictions, reaching $25\,\mathrm{m}°$

After optical verification, measurements have been repeated at the target tilt angles for both mirrors and verified using a purely electrical measurement. Linearity has been measured considering that only $90\,\%$ of the trace is used for projection. The figure of merit is extracted by taking the difference between the trace and a line fit, performing an average of traces acquired over a time frame of $1\,\mathrm{s}$ in order to filter noise contributions. Fig. 11 shows the linearity error obtained for both mirror 1 and 2 driven by $60\,\mathrm{Hz}$ and $120\,\mathrm{Hz}$ triangular waves with a retrace time equal to $10\,\%$ of the period. The maximum error, normalized to the full scale range, is within $\pm1\,\%$ and $\pm0.18\,\%$ for mirror 1 and 2 respectively when driven at $60\,\mathrm{Hz}$, while the error for mirror 2 remains within $\pm0.53\,\%$ of the full-scale tilt angle considering $85\,\%$ of the trace when driven at $120\,\mathrm{Hz}$. Note that for mirror 1 a residual ringing is visible on the error: it indicates that the phase margin is below $45°$, as expected due to the low-frequency effects of the modes and their compensation. The effect is not appreciated with mirror 2, which leads to a critically damped system consistently with the original design.

Finally, Fig.12 shows a statistic on six samples of mirror 2, which indicates the repeatability of the system implementation, and its capability to manage part-to-part variations of the device. The acquired peak-to-peak error remains limited within $\pm13\,\mathrm{m}°$, with a standard deviation of $3.7\,\mathrm{m}°$.

The obtained results are summarized in Table III, whereas Table IV lists the performance achieved by this work along with other works found in the literature, detailing either similar closed-loop applications, either open-loop solutions (marked with an asterisk) where a triangular signal is applied to the mirror. Although performing worse in terms of noise with respect to other solutions, our work shows a large achievable scanning angle and and a reduced closed-loop control error. Of particular interest is the last work in the list (marked with a dagger symbol), which shows a piezoelectric mirror with piezoresistive sensing, similarly to the devices discussed in this work. However, the discussed results rely on simulation data, and show a residual ramp-like error that is completely solved by our implementation thanks to double integration.

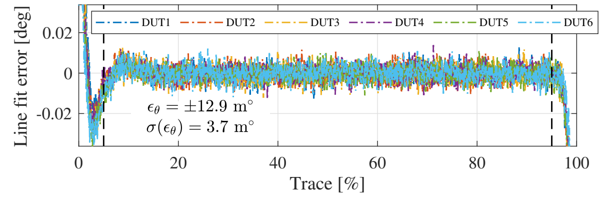

Fig. 12. Statistics of linearity for different samples of mirror 2, showing the robustness of the implemented system.

TABLE III
SYSTEM PERFORMANCE FOR THE TWO MIRRORS

Metric	M. 1	M. 2 (60 Hz)	M. 2 (120 Hz)
FOV	28°	32°	32°
Linear trace	90 %	90 %	85 %
Linearity	±1 %	±0.18 %	±0.53 %
Noise	26 m°	25.5 m°	25.5 m°
DR	60.6 dB	62 dB	62 dB

VI. Conclusion

This work presented a versatile closed-loop control strategy for quasi-static MEMS microscanners. The proposed solution is able to manage a wide range of mirror families, defined by the resonance frequency of their torsional mechanical mode, and driving frequencies. For a $60\,\mathrm{Hz}$ triangular actuation, the

TABLE IV
PERFORMANCE COMPARISON VS LITERATURE
ES: ELECTROSTATIC, EM: ELECTROMAGNETIC, PE: PIEZOELECTRIC, ET: ELECTROTHERMAL

	FOV	Linearity	Noise/Repeatability	Voltage
PE (this)	$32°$	$\pm 0.18\,\%$	$25.5\,\mathrm{m}°$	$40\,\mathrm{V}$
EM [6]	$1.6°$	$7\,\%$	$0.2°$	$5\,\mathrm{V}$
ES* [33]	$24.8°$	N/A	$\pm 3\,\mathrm{m}°$	$50\,\mathrm{V}$
ET* [34]	$18°$	$6\,\%$	N/A	$\approx 10\,\mathrm{V}$
ES [22]	$16°$	$\pm 0.4\,\%$	$\approx 2\,\mathrm{m}°$	$\approx 120\,\mathrm{V}$
ES* [18]	$24°$	$\pm 3.3\,\%$	$\approx 7\,\mathrm{m}°$	$\approx 100\,\mathrm{V}$
PZT† [28]	$32°$	$\pm 1.25\,\%$	N/A	$\approx 40\,\mathrm{V}$

solution works best at large native resonance frequencies, being capable of attaining linearity errors within $\pm 0.18\,\%$ of the full scale. However the system is proven to be able to manage smaller resonance frequencies with residual errors within $\pm 1\,\%$, as well as increased actuation frequencies up to $120\,\mathrm{Hz}$, with errors limited to $\pm 0.53\,\%$, while also achieving a very limited area occupation, as demonstrated by the implemented ASIC.

REFERENCES

[1] H. W. Yoo, R. Riegler, D. Brunner, S. G. Albert, T. Thurner, and G. Schitter, "Experimental evaluation of vibration influence on a resonant mems scanning system for automotive lidars," *IEEE Transactions on Industrial Electronics*, DOI 10.1109/TIE.2021.3065608, pp. 1–1, 2021.

[2] C.-d. Liao and J.-c. Tsai, "The evolution of mems displays," *IEEE Transactions on Industrial Electronics*, vol. 56, DOI 10.1109/TIE.2008.2005684, no. 4, pp. 1057–1065, 2009.

[3] Microsoft HoloLens 2: https://www.microsoft.com/en-us/hololens.

[4] A. D. Yalcinkaya, H. Urey, D. Brown, T. Montague, and R. Sprague, "Two-axis electromagnetic microscanner for high resolution displays," *Journal of Microelectromechanical Systems*, vol. 15, no. 4, pp. 786–794, Aug. 2006.

[5] Masanao Tani, Masahiro Akamatsu, Yoshiaki Yasuda, and Hiroshi Toshiyoshi, "A two-axis piezoelectric tilting micromirror with a newly developed pzt-meandering actuator," in *2007 IEEE 20th International Conference on Micro Electro Mechanical Systems (MEMS)*, DOI 10.1109/MEMSYS.2007.4432994, pp. 699–702, Jan. 2007.

[6] C.-C. Tsai, Z.-H. Li, Y.-T. Lin, and M. S.-C. Lu, "A closed-loop controlled cmos mems biaxial scanning mirror for projection displays," *IEEE Sensors Journal*, vol. 20, no. 1, pp. 242–249, 2020.

[7] G. Silva, F. Carpignano, F. Guerinoni, S. Costantini, M. De Fazio, and S. Merlo, "Optical detection of the electromechanical response of mems micromirrors designed for scanning picoprojectors," *IEEE Journal of Selected Topics in Quantum Electronics*, vol. 21, no. 4, pp. 147–156, Jul. 2015.

[8] J.-W. Cho et al., "Electrostatic 1D microscanner with vertical combs for HD resolution display," in *MOEMS and Miniaturized Systems VI*, vol. 6466, pp. 106 – 117, International Society for Optics and Photonics. SPIE, 2007.

[9] A. Frangi, A. Guerrieri, R. Carminati, and G. Mendicino, "Parametric resonance in electrostatically actuated micromirrors," *IEEE Transactions on Industrial Electronics*, vol. 64, DOI 10.1109/TIE.2016.2615274, no. 2, pp. 1544–1551, 2017.

[10] H. Urey, D. W. Wine, and T. D. Osborn, "Optical performance requirements for MEMS-scanner-based microdisplays," in *MOEMS and Miniaturized Systems*, vol. 4178, pp. 176 – 185, International Society for Optics and Photonics. SPIE, 2000.

[11] S. T. Holmström, U. Baran, and H. Urey, "Mems laser scanners: a review," *Journal of Microelectromechanical Systems*, vol. 23, no. 2, pp. 259–275, 2014.

[12] W. O. Davis, M. Beard, and R. Jackson, "Trajectory precision of micromachined scanning mirrors for laser beam scanning pico-projector displays," in *MOEMS and Miniaturized Systems XI*, vol. 8252, pp. 9 – 19, International Society for Optics and Photonics. SPIE, 2012.

[13] W. O. Davis, "Nonlinear air drag damping of torsional microscanners," in *2011 16th International Solid-State Sensors, Actuators and Microsystems Conference*, pp. 1424–1427, 2011.

[14] D. W. Wine, M. P. Helsel, L. Jenkins, H. Urey, and T. D. Osborn, "Performance of a biaxial MEMS-based scanner for microdisplay applications," in *MOEMS and Miniaturized Systems*, vol. 4178, pp. 186 – 196, International Society for Optics and Photonics. SPIE, 2000.

[15] H. Urey, "Mems scanners for display and imaging applications," in *Optomechatronic Micro/Nano Components, Devices, and Systems*, vol. 5604, pp. 218–229. International Society for Optics and Photonics, 2004.

[16] G. Schitter, P. J. Thurner, and P. K. Hansma, "Design and input-shaping control of a novel scanner for high-speed atomic force microscopy," *Mechatronics*, vol. 18, no. 5, pp. 282–288, 2008.

[17] K. Janschek, T. Sandner, R. Schroedter, and M. Roth, "Adaptive prefilter design for control of quasistatic microscanners," *IFAC Proceedings Volumes*, vol. 46, no. 5, pp. 197–206, 2013, 6th IFAC Symposium on Mechatronic Systems.

[18] R. Schroedter, K. Janschek, and T. Sandner, "Jerk and current limited flatness-based open loop control of foveation scanning electrostatic micromirrors," *IFAC Proceedings Volumes*, vol. 47, no. 3, pp. 2685–2690, 2014, 19th IFAC World Congress.

[19] K. Janschek, R. Schroedter, and T. Sandner, "Flatness-based open loop command tracking for quasistatic microscanners," ser. Dynamic Systems and Control Conference, vol. Volume 3, 10 2013.

[20] V. Milanović, A. Kasturi, J. Yang, and F. Hu, "Closed-loop control of gimbal-less MEMS mirrors for increased bandwidth in LiDAR applications," in *Laser Radar Technology and Applications XXII*, M. D. Turner and G. W. Kamerman, Eds., vol. 10191, pp. 157 – 169, International Society for Optics and Photonics. SPIE, 2017.

[21] R. Schroedter, M. Schwarzenberg, A. Dreyhaupt, R. Barth, T. Sandner, and K. Janschek, "Microcontroller based closed-loop control of a 2D quasi-static/resonant microscanner with on-chip piezo-resistive sensor feedback," in *MOEMS and Miniaturized Systems XVI*, W. Piyawattanametha and Y.-H. Park, Eds., vol. 10116, pp. 22 – 32, International Society for Optics and Photonics. SPIE, 2017.

[22] R. Schroedter, M. Roth, K. Janschek, and T. Sandner, "Flatness-based open-loop and closed-loop control for electrostatic quasi-static microscanners using jerk-limited trajectory design," *Mechatronics*, vol. 56, pp. 318–331, 2018.

[23] D. Brunner, H. W. Yoo, and G. Schitter, "Linear modeling and control of comb-actuated resonant mems mirror with nonlinear dynamics," *IEEE Transactions on Industrial Electronics*, vol. 68, DOI 10.1109/TIE.2020.2982124, no. 4, pp. 3315–3323, 2021.

[24] P. Frigerio, M. Gianollo, G. Pezzi, L. Molinari, A. Barbieri, M. Zamprogno, R. Carminati, N. Boni, and G. Langfelder, "Mitigating Hysteresis Effects in Open-loop-driven PZT MEMS Micromirrors With Piezoresistive Sensing," in *Transducers 2021 Conference*, 2021.

[25] A. Vergara, T. Tsukamoto, W. Fang, and S. Tanaka, "Feedback control of thin film pzt mems actuator with integrated buried piezoresistors," *Sensors and Actuators A: Physical*, vol. 332, DOI https://doi.org/10.1016/j.sna.2021.113131, 2021.

[26] A. Vergara, T. Tsukamoto, W. Fang, and S. Tanaka, "Pzt mems actuator with integrated buried piezoresistors for position control," in *2021 IEEE 34th International Conference on Micro Electro Mechanical Systems (MEMS)*, DOI 10.1109/MEMS51782.2021.9375422, pp. 626–629, 2021.

[27] A. Vergara, T. Tsukamoto, W. Fang, and S. Tanaka, "Integration of buried piezoresistive sensors and PZT thin film for dynamic and static position sensing of MEMS actuator," *Journal of Micromechanics and Microengineering*, vol. 30, DOI 10.1088/1361-6439/abb756, no. 11, Sep. 2020.

[28] A. Vergara, T. Tsukamoto, W. Fang, and S. Tanaka, "Feedback controlled pzt micromirror with integrated buried piezoresistors," in *2022 IEEE 35th International Conference on Micro Electro Mechanical Systems Conference (MEMS)*, DOI 10.1109/MEMS51670.2022.9699754, pp. 243–246, 2022.

[29] P. Frigerio, B. Di Diodoro, V. Rho, R. Carminati, N. Boni, and G. Langfelder, "Long-Term Characterization of a New Wide-Angle Micromirror With PZT Actuation and PZR Sensing," *Journal of Microelectromechanical Systems*, vol. 30, no. 2, pp. 281–289, 2021.

[30] B. J. G. Vautier and S. O. R. Moheimani, "Charge driven piezoelectric actuators for structural vibration control: issues and implementation," *Smart Materials and Structures*, vol. 14, no. 4, pp. 575–586, Jun. 2005.

[31] P. Frigerio, A. Barbieri, M. Zamprogno, and G. Langfelder, "Modeling and experimental verification of the impact of noise sources on projection accuracy of MEMS linear micromirrors for raster scanning applications," in *MOEMS and Miniaturized Systems XX*, vol. 11697, p. 1169716. International Society for Optics and Photonics, 2021.

[32] Polytec Microscope-based vibrometers. Online catalog: https://www.polytec.com/eu/vibrometry/products/microscope-based-vibrometers.

[33] W. Piyawattanametha, P. Patterson, D. Hah, H. Toshiyoshi, and M. Wu, "Surface- and bulk- micromachined two-dimensional scanner driven by angular vertical comb actuators," *Journal of Microelectromechanical Systems*, vol. 14, DOI 10.1109/JMEMS.2005.859073, no. 6, pp. 1329–1338, 2005.

[34] S. Pal and H. Xie, "Pre-shaped open loop drive of electrothermal micromirror by continuous and pulse width modulated waveforms," *IEEE Journal of Quantum Electronics*, vol. 46, DOI 10.1109/JQE.2010.2050864, no. 9, pp. 1254–1260, 2010.

Paolo Frigerio received his B.Sc. and M.Sc. degrees in Electronics engineering in 2016 and 2018 from Politecnico di Milano, Italy. During his M.Sc. thesis he worked on a temperature compensated Real-Time Clock. He is currently pursuing a Ph.D. in Information Technology at Politecnico di Milano, researching electronic systems for actuation and control of MEMS micromirrors.

Luca Molinari received the degree in Information Technology Engineering from Politecnico di Milano, Milan, Italy in 1997. From 1998 with STMicroelectronics he worked in the Audio Division on digital Class D amplifiers and audio DSP. In 2011 he joined the MEMS and Sensor Group where he is currently managing the divisional ASIC design group responsible of MEMS Actuators Drivers and control design for AR/VR, 3D sensing and LIDAR applications. He is author or co-author in 7 patents and 4 publications on Audio, DSP and MEMS drivers.

Andrea Barbieri received the degree in electronic engineering from the University of Pavia, Italy, in 2004. From 2004 to 2008 he worked with STMicroelectronics on mixed-signal ICs for wireless telecommunication. From 2008 with ST-Ericsson he specialized in sigma-delta conversion and low-noise acoustic interfaces. From 2013 he works with STMicroelectronics on the development of circuits for MEMS microphones. He is presently involved in the design of high-voltage driving and low-noise sensing circuits for MEMS micromirrors. He is co-author in 12 patents and 7 publications in the IEEE.

Marco Zamprogno received the degree in Electronic Engineering from Politecnico di Milano, Milan, Italy in 2001. From 2000 he works with STMicroelectronics. In 2013 he joined Audio, MEMS, and Sensor Group where he is presently working as Senior Member of the Technical Staff on the development of high-voltage drivers for MEMS micro-mirrors, laser diodes and piezoelectric actuators. He holds more than 25 patents and he is co-author of 10 publications. Since 2018 he's ESSCIRC TPC member.

Gianluca Mendicino received the M.Sc.degree in Physics from the Università degli Studi di Milano, Milan, Italy, 2015. During his M.Sc. studies, he worked on nuclear particle-phonon coupled states in the copper nucleus. He is currently a MEMS Validation Engineer in the MEMS Group, STMicroelectronics, Cornaredo, Italy, where he is working on the validation and industrialization of micromirror MEMS actuator.

Nicolò Boni received the M.Sc. degree in civil engineering from the Politecnico di Milano, Milan, Italy, in 2016. In his M.Sc. thesis, he worked on the nonlinear dynamic response of torsional micromirrors and their numerical simulation. He is currently a Design Engineer with the MEMS R&D Group, STMicroelectronics, Italy, where he is working in the development and industrialization of micromirror devices based on MEMS technology.

Giacomo Langfelder (M'12) received the Ph.D. degree in information technology from the Politecnico di Milano, Milan, Italy, in 2009. He is an Associate Professor of MEMS and Microsensors with the Politecnico di Milano. He is the author of more than 100 publications and has applied for more than ten patents. His research interests include sensors and related electronics. Dr. Langfelder has been a member of the TPC of various IEEE conferences since 2016.